Second harmonic generation in the presence of walk-off and group velocity mismatch

Marc Hanna, Michele Natile, Yoann Zaouter, Manuel Joffre, Patrick Georges

Second harmonic generation in the presence of walk-off and group velocity mismatch

Marc Hanna[1,*], **Michele Natile**[2], **Yoann Zaouter**[2], **Manuel Joffre**[3], **Patrick Georges**[1]

[1]Université Paris-Saclay, Institut d'Optique Graduate School, CNRS, Laboratoire Charles Fabry, 91127 Palaiseau, France
[2]Amplitude, 11 Avenue de Canteranne, Cité de la Photonique, 33600 Pessac, France
[3]Laboratoire d'Optique et Biosciences, Ecole Polytechnique, CNRS, INSERM, Institut Polytechnique de Paris, 91128 Palaiseau, France
[*]marc.hanna@institutoptique.fr

Abstract: We study a second-harmonic generation interaction geometry in the case where both group velocity mismatch and walk-off have significant impact. This results in a frequency-converted beam exhibiting pulse front tilt. Using the global response function of the crystal, we provide an analytical model that allows to predict the spatio-temporal structure of the second-harmonic wavepacket and verify its validity using numerical simulations and a simple experiment. Distinctive features of this geometry are the suppression of back-conversion and the ability to conserve the fundamental bandwidth in the space and time domains. Subsequent compensation of the pulse front tilt should allow efficient generation of ultrashort pulses in the deep ultraviolet.

1. Introduction

Second harmonic generation (SHG) was the first nonlinear optical phenomenon to be observed shortly after the invention of the laser [1]. Since then, it has proven invaluable to generate coherent radiation in wavelength ranges where available laser materials exhibit mediocre properties or are simply not available, in temporal regimes ranging from CW to femtosecond pulses. In particular, mature laser technologies generating beams in the near infrared based on neodymium- or ytterbium-doped materials can be used to produce high-power sources of light in the visible or UV ranges [2–4], after wavelength conversion through SHG. The efficiency of the process and the properties of the interaction and converted beams have been quite extensively described since the 1960s [5].

Two phenomena, walk-off and group-velocity mismatch (GVM), are essential in understanding SHG of short pulses that are tightly focused onto the nonlinear material. They are closely related and can be seen as dual versions in the space and time domains of the same effect [6]: walk-off is related to the first-order dependence of fundamental and/or second-harmonic wavevectors with respect to angular deviations (or equivalently transverse component of the wavevector) from the phase-matching angle. GVM is related to the first-order dependence of these same wavevectors with respect to optical frequencies. Walk-off and GVM are also closely related to the notions of angular and spectral acceptance respectively.

Theoretical descriptions and consequences of these effects have been available for decades in various levels of complexity. Since the first formalism describing SHG with focused Gaussian beam that included walk-off [5], other models have been developed to take into account GVM alone [7, 8]. An analytical model for the efficiency of SHG that takes both GVM and walk-off into account was also published in 2003 [9]. However, this work does not establish the space-time structure of the SHG beam, nor does it allow to predict its spatial and spectral widths.

Here we present a simple model that allows to predict the coupled space-time structure of the SHG beam in the presence of both walk-off and GVM. Although it has been recognized in the context of pulse characterization techniques [10] that the simultaneous presence of these effects leads to pulse front tilt (PFT), or equivalently angular dispersion, the implications have not been examined for SHG to our knowledge. Our model is established in the spatial and temporal frequency domain [6], as opposed to previous descriptions in the space / time domain [5, 7–9]. It matches the predictions of previous approaches, and also yields the explicit analytical solution which allows to predict SHG bandwidths, efficiency, and spatio-temporal beam structure in a rather general case, providing an analytical ground for what has been observed experimentally [11, 12]. One important consequence is that in the presence of strong GVM and walk-off, back conversion to the fundamental beam is suppressed in both the space and time domains, allowing to reach large conversion efficiencies. Full 3D numerical simulations are performed to confirm the validity of this model, making it a useful tool to design efficient frequency conversion stages for ultrashort pulses, and an experimental confirmation of the presence of strong space-time couplings in the SHG beam is presented. Practical consequences are expected to be important for the generation of short pulses in the UV and DUV ranges, where both walk-off and GVM parameters have large values, with possible applications to material processing and experiments involving the generation of photoelectrons.

2. Intuitive description in the space-time domain

A simple picture in the space-time domain allows to establish the presence of PFT in the SHG beam and determine its value, as shown in Fig. 1. Consider an input fundamental wavepacket entering at the left side of the nonlinear crystal that exhibits both walk-off and GVM. During propagation, at each location, this wavepacket triggers a second order polarization that radiates the SHG beam. This beam propagates at a usually lower group velocity, at an angle determined by the walk-off in the considered crystal. Fig. 1 shows in red the position of these individual SHG beamlets at the time corresponding to the fundamental beam leaving the nonlinear crystal. These beamlets are arranged in a line, with a PFT angle γ given by

$$\tan\gamma = \frac{v_{g1} - v_{g2}\cos\rho}{v_{g2}\sin\rho}, \tag{1}$$

where ρ is the walk-off angle, and v_{g1} and v_{g2} are the group velocities of the fundamental and SHG pulses respectively. For sufficiently small values of the walk-off angle, this reduces to

$$\tan\gamma \approx v_{g1}\frac{\mathrm{GVM}}{\rho}, \tag{2}$$

where the GVM parameter is defined by $\mathrm{GVM} = 1/v_{g2} - 1/v_{g1}$. The factor GVM/$\rho$ is the PFT parameter in units of s/m, and only depends on the phase matching geometry. The presence of PFT in the SHG beam is, to our knowledge, not mentioned in previous papers describing efficient generation using thick crystals where GVM and walk-off are both present [11, 12]. In general, when the SHG beam quality and SHG efficiency is the major concern, configurations with large GVM or walk-off are avoided. It is however at the basis of some pulse characterization techniques that use sum-frequency mixing [10]. Although the PFT can hinder further applications, it is well known that it is equivalent to angular dispersion [13, 14], and can be controlled, and removed, using angularly dispersive optical components such as prisms and gratings. This would correspond to the inverse of a technique that has been studied over the last 25 years [15–19], where the idea is to generate SHG or perform another nonlinear frequency mixing from an input pulse exhibiting PFT, in order to maximize the phase-matching bandwidth.

Although this simple picture in the time-space domain allows to evaluate the PFT and PFT angles, it remains unclear what the detailed structure of the SHG beam is. For instance, what is its optical bandwidth, or how does this beam diffract in the far field? To get more insight into this process, and be able to predict such properties, we now describe this interaction in more details using a simple analytical model.

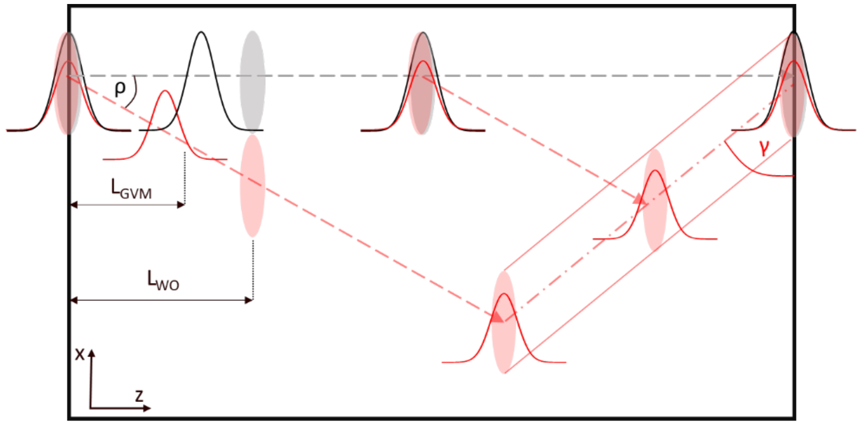

Fig. 1. Illustration of the origin of the pulse front tilt in the SHG beam in the presence of GVM and walk-off. The black/grey colors are associated to the fundamental beam, and the red color is associated to the SHG beamlets. The GVM and walk-off characteristic lengths, corresponding to separation of the fundamental and SHG wavepackets in time and space respectively, are also illustrated (respectively L_{GVM} and L_{WO}).

3. Simple model in the wavevector-spectral domain

The model we develop here is based on the spatio-temporal generalization of the global multidimensional response function, hereafter denoted Ξ. This approach, discussed earlier within the plane-wave approximation [20], has been used previously in the context of broadband SHG [21] and multidimensional spectroscopy [22,23]. While a complete theoretical development is provided in the Appendix, this section focuses on the most relevant physical effects. As shown in Fig. 1, we assume that the fundamental and SHG pulses propagate in the z direction, and we keep only one spatial transverse dimension, x, chosen so that the xz plane contains the optical axis. The complex electric field is written as a function of its 2D Fourier transform according to

$$E_\ell(z,x,t) = \iint E_\ell(z,k_x,\omega)e^{i(k_x x-\omega t)}\frac{dk_x}{2\pi}\frac{d\omega}{2\pi}, \tag{3}$$

with $\ell = 1$ for the fundamental and $\ell = 2$ for the second harmonic. Second-order effects such as diffraction in the space domain or group-velocity dispersion (GVD) in the time domain are neglected for simplicity, although they can be readily included as shown in the Appendix. Pump depletion is also neglected so that propagation of the fundamental pulse complex field is simply described by

$$E_1\left(z,k_x,\omega\right) = E_1\left(0,k_x,\omega\right)\ \exp\left(ik_1(k_x,\omega)z\right), \tag{4}$$

where k_1 is the wavevector of the fundamental wavepacket. We write the second-harmonic complex field as $E_2\left(z,k_x,\omega\right) = A_2\left(z,k_x,\omega\right)\ \exp\left(ik_2(k_x,\omega)z\right)$, where $k_2(k_x,\omega)$ is the wavevector of the SHG wavepacket, and $A_2\left(z,k_x,\omega\right)$ is a slowly-varying envelope. As shown in the Appendix, the propagation of the SHG pulse is described within the paraxial wave approximation by

$$\frac{\partial A_2(z,k_x,\omega)}{\partial z} = \frac{i\omega}{2n_2\varepsilon_0 c}P^{(2)}\left(z,k_x,\omega\right)\ \exp\left(-ik_2(k_x,\omega)z\right), \tag{5}$$

where n_2 is the refractive index at the SHG center frequency, ε_0 is the vacuum permittivity, and c is the speed of light in vacuum. The second-order nonlinear polarization $P^{(2)}$ is given by:

$$P^{(2)}\left(z,x,t\right) = \frac{\varepsilon_0\chi^{(2)}}{2}E_1^2(z,x,t). \tag{6}$$

Fourier transform and substitution of this expression in the propagation equation (5) leads, after integrating over z, to the following expression for the SHG pulse envelope

$$A_2(z,k_x,\omega) = \iint \Xi(k_x,k_{x1},\omega,\omega_1)E_1(k_{x1},\omega_1)E_1(k_x-k_{x1},\omega-\omega_1)\frac{dk_{x1}}{2\pi}\frac{d\omega_1}{2\pi}, \quad (7)$$

where the dropped dependence on z in E_1 means that it is taken at $z = 0$. In the above equation, we have introduced the multidimensional spatio-temporal response function $\Xi(k_x,k_{x1},\omega,\omega_1)$, expressed below as a function of the wavevector mismatch, Δk:

$$\Xi(k_x,k_{x1},\omega,\omega_1) = \frac{i\omega\chi^{(2)}}{4n_2c}\frac{\exp\left(i\Delta k(k_x,k_{x_1},\omega,\omega_1)\,z\right)-1}{i\Delta k(k_x,k_{x_1},\omega,\omega_1)}. \quad (8)$$

The wavevector mismatch Δk is itself defined as

$$\Delta k\left(k_x,k_{x_1},\omega,\omega_1\right) = k_1\left(k_{x_1},\omega_1\right)+k_1\left(k_x-k_{x_1},\omega-\omega_1\right)-k_2\left(k_x,\omega\right). \quad (9)$$

The result of Eq. (7) is somewhat similar to previous approaches [5,9] but is formulated here in Fourier space. We now start by assuming perfect phase matching ($\Delta k = 0$) as a reference point for later derivations. In this case, $\Xi = i\omega\chi^{(2)}z/(4n_2c)$ and the second harmonic pulse is simply given by

$$A_{2,PM}\left(z,k_x,\omega\right) = z\frac{i\omega\chi^{(2)}}{4n_2c}\iint E_1\left(k_{x_1},\omega_1\right)E_1\left(k_x-k_{x_1},\omega-\omega_1\right)\frac{dk_{x_1}}{2\pi}\frac{d\omega_1}{2\pi}. \quad (10)$$

We recover the fact that the intensity of the SHG beam grows like z^2. SHG can be interpreted as a summation of sum-frequency processes both in the temporal and spatial frequency domains. In the case where the fundamental wavepacket E_1 is a Gaussian function in space and time, the autoconvolution operation results in a SHG pulse with a spectral width multiplied by $\sqrt{2}$, and a spatial frequency width multiplied by the same factor. This corresponds to a pulsewidth and a beam radius divided by $\sqrt{2}$, a well-known result that stems from the quadratic polarization term.

Let us now consider the case where the wavevectors exhibit first-order dependencies on ω and k_x as follows:

$$k_1(k_x,\omega) = k_1(\omega_0)+\frac{\partial k_1}{\partial\omega}(\omega-\omega_0) \quad (11)$$

$$k_2(k_x,\omega) = k_2(2\omega_0)+\frac{\partial k_2}{\partial\omega}\left(\omega-2\omega_0\right)+\frac{\partial k_2}{\partial k_x}k_x. \quad (12)$$

In this case, for simplicity, we have considered a type I (ooe) SHG where the fundamental beam is polarized along the ordinary axis of the nonlinear crystal, so that its k-vector does not depend on k_x or equivalently the phase matching angle. However, the SHG beam is polarized along the extraordinary axis, and therefore exhibits walk-off. Note that this analysis can be extended to other phase-matching geometries. The phase mismatch is thus given by:

$$\Delta k\left(k_x,k_{x_1},\omega,\omega_1\right) = \left(\frac{\partial k_1}{\partial\omega}-\frac{\partial k_2}{\partial\omega}\right)(\omega-2\omega_0)-\frac{\partial k_2}{\partial k_x}k_x = GVM\times\Omega-\rho\times k_x, \quad (13)$$

where we have identified the GVM parameter and walk-off angle, and $\Omega = \omega - 2\omega_0$. We can see that, to first order, Δk does not depend on ω_1 and k_{x_1}, so that the response function $\Xi(k_x,k_{x1},\omega,\omega_1) = \Xi(k_x,\omega)$ can be taken out of the integral in Eq. (7). The response function then merely acts as a filter that will attenuate (k_x,Ω) components that are not phase matched. As a result, the emitted SHG field can be written as:

$$A_2\left(z,k_x,\Omega\right) = A_{2,PM}(z,k_x,\Omega)\exp\left(i\frac{\Delta kz}{2}\right)\mathrm{sinc}\left(\frac{\Delta kz}{2}\right). \quad (14)$$

The SHG field can therefore be decomposed into the product of the perfectly phase-matched result, that occupies a region of the (k_x, Ω) space, with the standard sinc function describing phase matching effects. The additional phase term is linear in ω and k_x, and therefore simply corresponds to a shift in the time and space domains. To determine the region of the (k_x, Ω) space that corresponds to perfect phase matching, we set $\Delta k = 0$ and find

$$k_x = \frac{GVM}{\rho}\Omega, \tag{15}$$

describing a linear angular dispersion that is coherent with the PFT established in Eq. (2).

3.1. Spectral and wavevector widths

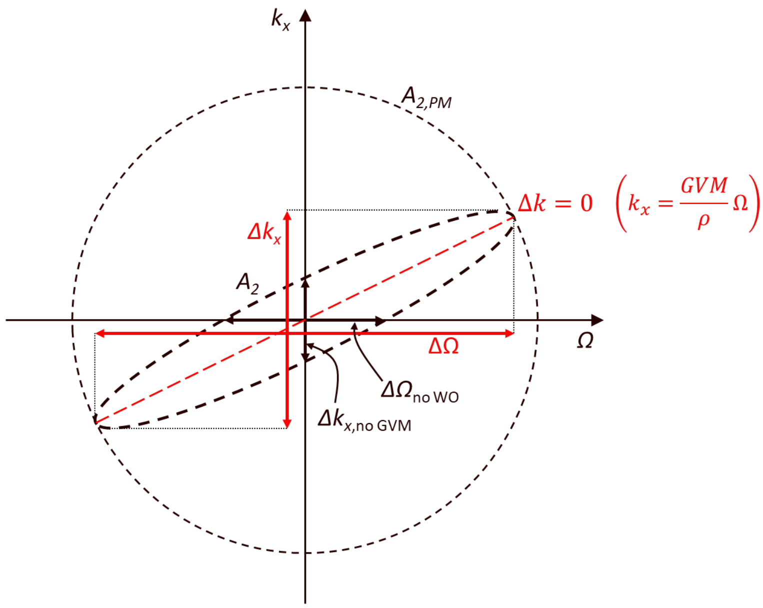

Fig. 2. Schematic of the (k_x, Ω) plane showing the extent of the second-order polarization term resulting in $A_{2,PM}$ and the $\Delta k = 0$ line in the presence of both walk-off and GVM. The dashed-line ellipse represents schematically A_2, obtained by multiplying $A_{2,PM}$ by the response function. The different spectral and angular widths are also shown.

In addition to recovering this result, this simple model allows to compute the overall widths of the radiated SHG beam. For this, Fig. 2 helps visualizing the situation in the (k_x, Ω) domain. The spatio-temporal response function sinc $(\Delta k z/2)$ acts as a filter in the (k_x, Ω) plane, resulting in the SHG field represented by the dashed-line ellipse. Let us assume that the input fundamental beam is Gaussian in space and time:

$$E_1(x,t) \propto \exp\left(-\frac{t^2}{2\Delta t^2} - \frac{x^2}{2\Delta x^2} - i\omega_0 t\right) \longleftrightarrow E_1(k_x, \Omega) \propto \exp\left(-\frac{(\omega-\omega_0)^2}{2\Delta\omega^2} - \frac{k_x^2}{2\Delta k_x^2}\right), \tag{16}$$

with widths in the space and time domains verifying $\Delta t\ \Delta\omega = 1$ and $\Delta x\ \Delta k_x = 1$. The experimentally used full width at half maximum (FWHM) pulse duration Δt_{FWHM} and beam waist radius w are related to these widths by $\Delta t_{FWHM} = 2\sqrt{\ln 2}\,\Delta t$ and $w = \sqrt{2}\Delta x$. As already mentioned, in this case, the perfectly phase matched SHG field is given by the autoconvolution of the 2D Gaussian function, and therefore

$$\left|A_{2,PM}\left(z,k_x,\Omega\right)\right|^2 \propto \exp\left(-\frac{\Omega^2}{2\Delta\omega^2}-\frac{k_x^2}{2\Delta k_x^2}\right). \tag{17}$$

The coordinates of half intensity of this pulse in the 2D (k_x,Ω) plane are given by

$$\Delta t^2\Omega^2+\Delta x^2 k_x^2 = 2\ln 2 \tag{18}$$

The overall full widths at half maximum (FWHM) in the Fourier domains are obtained along the $\Delta k = 0$ line, yielding the following results:

$$\Delta\Omega_{FWHM} = \frac{2\sqrt{2\ln 2}}{\sqrt{\Delta t^2+GVM^2\frac{\Delta x^2}{\rho^2}}} \tag{19}$$

$$\Delta k_{x\ FWHM} = \frac{2\sqrt{2\ln 2}}{\sqrt{\Delta x^2+\rho^2\frac{\Delta t^2}{GVM^2}}}. \tag{20}$$

These equations formally establish an experimental observation that was reported several times [7, 12] with the following qualitative argument: in the presence of significant walk-off, instead of being determined by the overall nonlinear medium length, the spectral width is related to the walk-off length $L_{WO} = \Delta x/\rho$, because the fundamental and SHG fields interact coherently only over this distance. Symmetrically, the angular spectrum is determined by the GVM length $L_{GVM} = \Delta t/GVM$.

If we assume $k_x = 0$, corresponding to a large, collimated beam for which walk-off can be neglected, the spectral acceptance is limited by the sinc term instead of the input beam imprint in the (k_x,Ω) plane along the $\Delta k = 0$ line. In this case we recover the usual spectral acceptance

$$\Delta\Omega_{\text{no WO}} = \frac{2\pi\ 0.886}{GVM\ L}, \tag{21}$$

where L is the crystal length. Similarly, if we assume $\Omega = 0$, corresponding to a narrowband fundamental pulse, the angular acceptance is given by

$$\Delta \mathrm{k}_{x\ \text{no GVM}} = \frac{2\pi\ 0.886}{\rho\ L}. \tag{22}$$

3.2. Efficiency

This simple model also allows to evaluate the efficiency in the simultaneous presence of GVM and walk-off, a question that was already answered in previous work [9]. Here we show that the results are coherent with the literature and cast in a way that makes the symmetry between time and space clearer. To compute the efficiency, we must take the magnitude squared of Eq. (14) and integrate it over Ω and k_x. We define the efficiency of the perfectly phase-matched process as $\eta_{PM} = \eta_0 L^2$, and assume that the distribution of the wavepacket in the (k_x,Ω) plane is separable as a Gaussian function along the ellipse major axis and a sinc function along the minor axis. This is equivalent to saying that at least one of the effects, among WO and GVM, is strong enough to significantly reduce the spectral or angular acceptance. In this case the efficiency is found to be given by

$$\eta = \sqrt{2\pi}\eta_0\frac{L_{WO}L_{GVM}}{\sqrt{L_{WO}^2+L_{GVM}^2}}L. \tag{23}$$

The efficiency is now linear with propagation distance, a well-known result, and limited by an effective coherent interaction length that depends symmetrically on the walk-off and GVM lengths. We now turn to numerical simulations to validate the predictions of this simple model both in terms of the amount of PFT present in the output SHG beam and its angular and spectral distribution.

4. Numerical simulations

The numerical model is based on two envelope propagation equations [24] for the fundamental and SHG beams respectively, coupled through the second-order nonlinear polarization corresponding to the specific wave-mixing of interest. These fields are three-dimensional *E(x,y,t)* and propagated in the direction z using a split-step Fourier method: linear effects such as diffraction and dispersion are accounted for in the Fourier domain, while nonlinear effects are implemented in the direct space, over successive longitudinal propagation steps [25]. The wavevectors dependence on frequency and angle for each field are calculated using the full Sellmeier equations of the considered material [26]. This results in a model where dispersion to all orders (therefore including phase matching, GVM and GVD), walk-off, diffraction, and second-order nonlinear effects are completely taken into account. Pump depletion will therefore be observed for a sufficiently efficient interaction. Third-order nonlinear effects are also included but play a negligible role at the considered intensities.

As a starting point, we consider an input Gaussian fundamental pulse at 515 nm with a FWHM pulsewidth of 300 fs, and a beam waist radius (at $1/e^2$ in intensity) of 25 µm located at the center of the crystal. This pulse is launched into an 8 mm-long BBO crystal at a phase matching angle of θ=49.8°, corresponding to type I (ooe) phase matching for SHG. The confocal parameter corresponding to this pump beam radius in the crystal is 12.6 mm, while the GVD values at the pump and SHG wavelengths are 140 fs^2/mm and 460 fs^2/mm. As a result, diffraction and GVD have a limited impact on propagation.

The GVM parameter and walk-off angle in this situation are 630 fs/mm and 85 mrad. Over the 8 mm-long crystal, this translates into a delay between fundamental and SHG pulses of 5 ps and an overall lateral beam displacement of 680 µm, corresponding to very pronounced GVM and walk-off effects.

Figure 3 shows the spatio-temporal structure of the output SHG beam, along with integrated profiles in the time domain and along the critical phase matching direction x, obtained both from the analytical analysis of section 3 using Eq. (14), and from the full simulation with a very low input energy of 0.1 nJ, where pump depletion is negligible. The pulse front tilt expected from the simple argument of section 2 is clearly observed, with a PFT of 7.4 ps/mm. The analytical and simulation results are in very good agreement, except for the signal enhancement around $x = 0$ (and hence $t = 0$) due to pump beam size variations that are not taken into account in the analytical model. The observed linear coupling in the space-time domain is mirrored in the Fourier space-time domain, corresponding to angular dispersion.

In the remainder of this section, the input pulse energy is set to 5 nJ. The simulation results are shown in Fig. 4. In this case, in addition to the spatio-temporal structure, pump depletion causes the intensity of the SHG beam to increase gradually over time, because the SHG beamlets generated at the beginning of propagation, when the pump intensity is the highest, are delayed the most. In this case, the overall efficiency is 56%. This high value illustrates a distinctive feature of this frequency conversion geometry: because GVM and walk-off separate the fundamental and SHG radiations in time and space over rather small propagation distances compared to the crystal length, back-conversion, which supposes a coherent interaction, is suppressed.

The output SHG beam profiles in the near and far fields are shown in Fig. 5. As expected, the SHG beam at the output facet of the crystal exhibits a strongly asymmetric beam profile induced

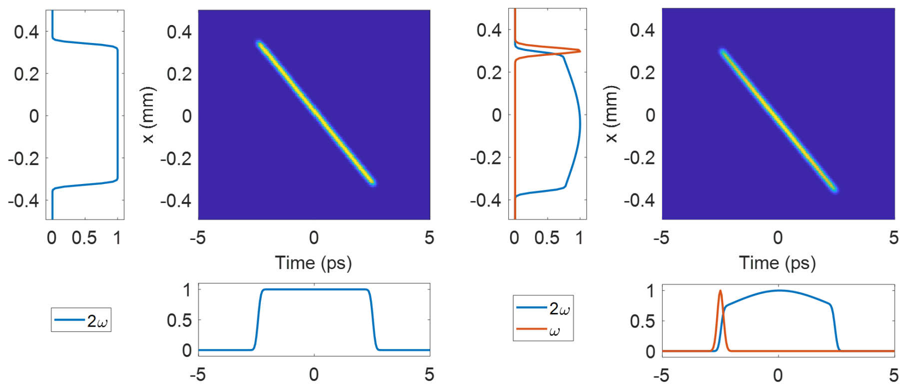

Fig. 3. Left: Spatio-temporal structure of the output SHG beam obtained from the analytical model (Fourier transform of Eq. (14)), and projections on the time and space axes (blue). Right: Same plot obtained from full numerical simulations at an input energy of 0.1 nJ, the red curve corresponds to the fundamental pulse at the output of the crystal.

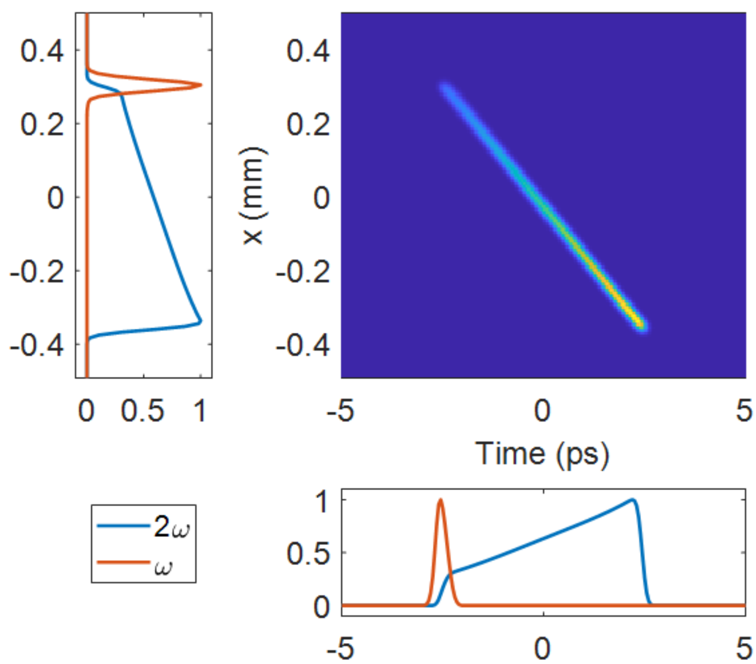

Fig. 4. Spatio-temporal structure of the output SHG beam obtained from full numerical simulations at an input energy of 5 nJ, and projections on the time and space axes (blue). The red curve corresponds to the fundamental pulse at the output of the crystal.

by the walk-off. However, contrary to the situation where GVM is negligible, this elongated profile in the near field does not translate into an equivalently elongated profile in the far field, with interchanged axes. The reason for this was identified, for example in [16]: because of the space-time coupling, wavepackets with PFT exhibit diffraction properties that are related to the instantaneous size of the beam rather than the time-integrated one, leading to stronger diffraction.

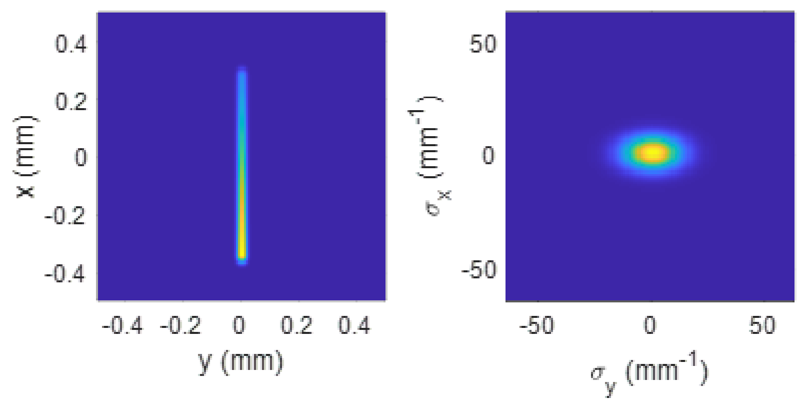

Fig. 5. Output SHG beam (left) and corresponding far field (right).

To get more physical insight into the behavior of SHG output spectral width and far-field width as a function of input parameters of the pump pulse such as pulsewidth and beam size, the model is used repeatedly while scanning one parameter. From the starting point, we first vary the input beam radius with values of 25 µm, 50 µm, and 100 µm. To keep the peak intensity constant, the pump pulse energy is set to 5 nJ, 20 nJ, and 80 nJ respectively. The SHG output spectrum, integrated over space, is shown in Fig. 6 (left). As expected from the analytical analysis, the spectral width is reduced as the input beam size increases, with values of 0.35 nm, 0.24 nm, and 0.14 nm. The results given by Eq. (19) are 0.37 nm, 0.26 nm, and 0.14 nm, in excellent agreement. For these situations where the walk-off displacement is much larger than the input beam size, the spectral width scales like the inverse of the input beam size. This is in line with experimental observations [7, 12], and the following explanation: as the length over which fundamental and SHG radiations interact coherently in the space domain L_{WO} increases, the spectral width is reduced because of the limited spectral acceptance of the crystal. However, for small initial beam sizes, the SHG pulse can be generated over the full input bandwidth, yielding a way to efficiently convert short pulses even in the presence of a large GVM, or equivalently a small spectral acceptance.

Symmetrically, from the starting point, we vary the pump pulsewidth with values of 300 fs, 600 fs, and 1200 fs, and pulse energies scaled to 5 nJ, 10 nJ, and 20 nJ respectively. Figure 6 (right) shows the time-integrated SHG far fields, yielding a result expected from Eq. (20): as the length over which fundamental and SHG radiations interact coherently in the time domain L_{GVM} increases, the angular width is reduced because of the limited angular acceptance of the crystal. However the full input wavevector spectrum can be converted if a sufficiently small pulsewidth is used at the input. The spatial frequency FWHM observed in simulations are 12 mm^{-1}, 7.0 mm^{-1} and 3.8 mm^{-1}, while Eq. (20) yields values of 12 mm^{-1}, 7.2 mm^{-1}, and 3.8 mm^{-1}, again in excellent agreement.

5. Experimental confirmation of the presence of angular dispersion

Finally, we perform an experiment to evidence the presence of PFT, or equivalently angular dispersion, in the output SHG beams when both GVM and walk-off play an important role. Starting from an ytterbium-doped femtosecond laser system at 1030 nm, we generate 300 fs

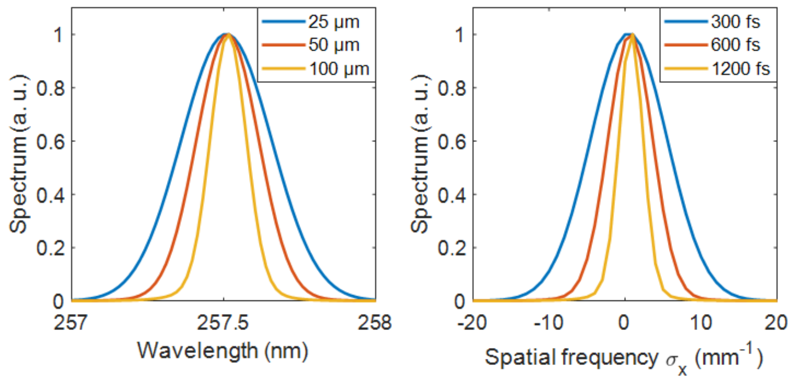

Fig. 6. Output SHG spectrum for input beam radii of 25, 50, and 100 µm (left). Output SHG wavevector spectrum for input pulse durations of 300, 600, and 1200 fs (right)

pulses at 515 nm in a first type I SHG stage using a 4 mm-long LBO crystal. These pulses are then focused onto a beam diameter of approximately 60 µm inside a 9.4 mm-long BBO crystal cut for type I SHG at 515 nm to generate a beam at 257 nm. These conditions approximately match the situation considered in the numerical simulations section.

The near field of the beam generated at 257 nm is measured by imaging the output facet of the nonlinear crystal onto a camera, and is displayed in Fig. 7. The strong beam asymmetry shown by the simulation in Fig. 5 is clearly observed. The spot that appears on top of the line is the fundamental beam at 515 nm. The far-field, measured using the same camera by removing the imaging lens, is shown in Fig. 7, and is also in qualitative agreement with the simulations. In particular, the difference in size between the vertical and horizontal directions is not at all as pronounced as in the near-field, because of the presence of strong spatio-temporal couplings.

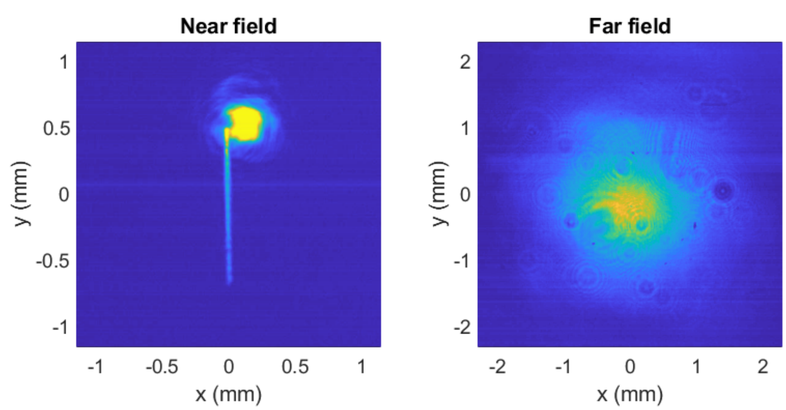

Fig. 7. Measured near-field (left) and far-field (right) profiles of the DUV beam.

To obtain a quantitative estimation of the PFT, we let the generated UV beam propagate to the far field and a spectrometer coupled to a 50 µm diameter multimode fiber mounted on a translation stage is positioned 31 cm away from the crystal. This allows to measure the spatial chirp at this location, a consequence of the angular dispersion. The data is plotted as spectra as a function of deviation angle from the beam center.

Figure 8 shows the result of this measurement. The left panel shows that the central wavelength

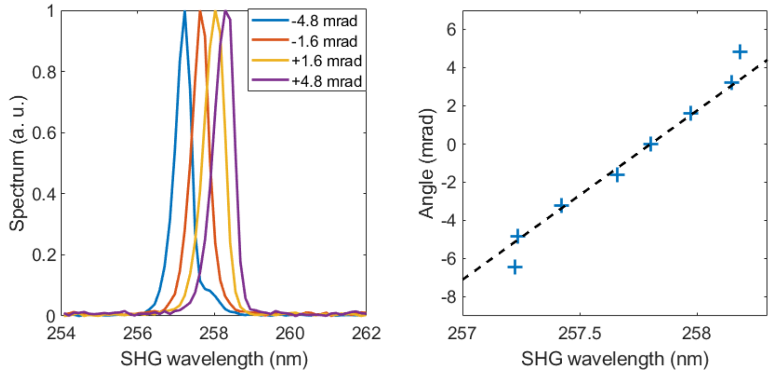

Fig. 8. Left: Measured SHG spectra in the far field at deviations angle varying from -4.8 mrad to +4.8 mrad from the optical axis in the critical phase matching plane. Right: deviation angle as a function of centroid wavelength, with a slope of 9.0 mrad/nm.

shifts as the fiber is translated in the UV beam, as expected for an angularly dispersed beam. The right panel shows the angular deviation as a function of centroid wavelength, with an experimentally measured angular dispersion of 9.0 mrad/nm. This value is very close to the theoretically expected one of $\partial\theta/\partial\lambda = PFT \times c/\lambda_0 = 8.6$ mrad/nm. This simple experiment therefore confirms the spatio-temporal structure of the SHG beam.

6. Conclusion

To conclude, we have presented an analytical model that predicts the spatio-temporal structure of SHG beams when both GVM and walk-off play a significant role. We show that a pulse front tilt is imparted onto the beam, as the fundamental and SHG wavepackets separate in both space and time. This separation implies that the coherent interaction length is limited both in the time and space domains, therefore suppressing the possibility for back conversion. As a result, it is possible to obtain high SHG efficiencies using this scheme, even for pulses exhibiting a bandwidth that exceeds the spectral acceptance of the crystal. The output beam PFT can be compensated using standard optical elements that introduce angular dispersion such as gratings and prisms. When pump depletion is negligible, the output pulses exhibit a square-shaped profile in the time domain and in the direction of critical phase-matching. The onset of pump depletion causes these profiles to become inhomogeneous. To generate more spatially symmetric profiles, beam reshaping techniques using e. g. cylindrical lenses could be used.

This nonlinear interaction geometry bears some similarities with broadband phase matching techniques based on the introduction of pulse front tilt in the input interacting beams. These techniques also require compensation of the output PFT in the generated beam. However, in the case studied here, there is no need for spatio-temporal beam management of the input pulses. The lack of back-conversion is also a distinctive feature, that avoids bandwidth-limiting effects and related spectral and spatial profiles distortions.

The nonlinear interaction geometry described here is particularly relevant for conversion to the UV / DUV ranges, where indices of refraction of nonlinear crystals vary rapidly both as a function of wavelength and angle, yielding large values of walk-off and GVM parameters. Subsequent PFT compensation might therefore prove useful to efficiently convert broad bandwidth visible pulses to the UV while conserving a short pulse duration. The peculiar properties of this interaction geometry call for a reexamination of available nonlinear crystals properties in this wavelength range, since GVM and walk-off are no longer mechanisms that limit the focusing and/or spectral bandwidth.

Appendix

In this appendix, we provide a detailed spatio-temporal calculation in Fourier space, including two transverse spatial coordinates and the effects of diffraction and group-velocity dispersion. We write the complex electric field, $E_\ell(\vec{r},t)$, using its 4D Fourier transform

$$E_\ell(\vec{r},t) = \frac{1}{(2\pi)^4} \iiiint E_\ell(\vec{k},\omega)\exp(i(\vec{k}\cdot\vec{r}-\omega t))d^3k d\omega. \tag{24}$$

Within the non-depleted pump approximation, the fundamental field $E_1(\vec{k},\omega)$, assumed here to be an ordinary wave, simply obeys the linear propagation equation

$$(-(k_x^2+k_y^2+k_z^2)+k_1(\omega)^2)E_1(k_x,k_y,k_z,\omega) = 0, \tag{25}$$

where $k_1(\omega) = n_o(\omega)\omega/c$. Within the paraxial wave approximation, we write

$$E_1(k_x,k_y,z,\omega) = A_1(k_x,k_y,z,\omega)e^{ik_1(\omega)z}, \tag{26}$$

where $A_1(k_x,k_y,z,\omega)$ is an envelope assumed to vary slowly with respect to z, the propagation axis. The corresponding expression in Fourier space simply reads $E_1(k_x,k_y,k_z,\omega) = A_1(k_x,k_y,k_z-k_1(\omega),\omega)$, or equivalently $A_1(k_x,k_y,\kappa_z,\omega) = E_1(k_x,k_y,k_1(\omega)+\kappa_z,\omega)$, where $\kappa_z = k_z - k_1(\omega)$ is small with respect to $k_1(\omega)$. The paraxial wave approximation consists of keeping terms up to first order in κ_z and up to second order in k_x and k_y. Replacing in Eq. (25) and neglecting the term in κ_z^2, we obtain

$$(-k_x^2-k_y^2-2k_1(\omega)\kappa_z)A_1(k_x,k_y,\kappa_z,\omega) = 0, \tag{27}$$

or

$$i\kappa_z A_1(k_x,k_y,\kappa_z,\omega) = -i\frac{k_x^2+k_y^2}{2k_1(\omega)}A_1(k_x,k_y,\kappa_z,\omega). \tag{28}$$

Going back to real space for coordinate z, we obtain

$$\frac{\partial A_1}{\partial z} = -i\frac{k_x^2+k_y^2}{2k_1(\omega)}A_1(k_x,k_y,z,\omega), \tag{29}$$

which immediately yields

$$A_1(k_x,k_y,z,\omega) = A_1(k_x,k_y,\omega)\exp\left(-i\frac{k_x^2+k_y^2}{2k_1(\omega)}z\right). \tag{30}$$

We thus recover the well-known expression of the electric field in wavevector space within the paraxial wave approximation,

$$E_1(k_x,k_y,z,\omega) = E_1(k_x,k_y,\omega)\exp\left(ik_1(\omega)z - i\frac{k_x^2+k_y^2}{2k_1(\omega)}z\right), \tag{31}$$

where the dropped dependence on z in E_1 means that we are considering the field at the entrance of the crystal, $E_1(k_x,k_y,\omega) = A_1(k_x,k_y,\omega) = E_1(k_x,k_y,0,\omega)$. Eq. (31) includes the effects of both diffraction and dispersion and allows to compute the fundamental field $E_1(x,y,z,t)$ through a 3D Fourier transform, so that the second-order polarization $P^{(2)}(x,y,z,t)$ can be readily calculated, as well as its counterpart in Fourier space.

Let us now turn to the propagation of the second harmonic. Assuming that the crystal axis lies in the xz plane, the propagation equation now reads

$$(-(k_x^2 + k_y^2 + k_z^2) + k_2(k_x,\omega)^2)E_2(k_x,k_y,k_z,\omega) = -\frac{\omega^2}{\epsilon_0 c^2} P^{(2)}(k_x,k_y,k_z,\omega), \tag{32}$$

where we have included the second-order polarization as a known source term. Note that, due to the crystal anisotropy, the quantity $k_2(k_x,\omega) = n_e(\theta(k_x),\omega)\omega/c$ depends on the transverse component k_x. Indeed, within the paraxial wave approximation we can write $\theta = \theta_0 - k_x/k_2(\omega)$, where θ_0 is the angle between the z axis and the optical axis and $k_2(\omega) = n_e(\theta_0,\omega)\omega/c$. The first-order derivative of the wavevector with respect to k_x reads

$$\frac{\partial k_2}{\partial k_x} = \frac{\omega}{c}\frac{\partial n_e(\theta)}{\partial \theta}\frac{\partial \theta}{\partial k_x} = \tan\rho, \tag{33}$$

where we have used the well-known relation verified by the tangent of the walk-off angle, ρ,

$$\tan\rho = -\frac{1}{n_e(\theta)}\frac{dn_e(\theta)}{d\theta} = n_e(\theta)^2\left(\frac{1}{n_e^2} - \frac{1}{n_o^2}\right)\sin 2\theta. \tag{34}$$

Proceeding as for the fundamental beam, we consider the envelope $A_2(k_x,k_y,\kappa_z,\omega) = E_2(k_x,k_y,k_2(k_x,\omega)+\kappa_z,\omega)$, so that Eq. (32) becomes

$$-(k_x^2 + k_y^2 + 2k_2(k_x,\omega)\kappa_z)A_2(k_x,k_y,\kappa_z,\omega) = -\frac{\omega^2}{\epsilon_0 c^2}P^{(2)}(k_x,k_y,k_2(k_x,\omega)+\kappa_z,\omega) \tag{35}$$

or

$$\begin{aligned} i\kappa_z A_2(k_x,k_y,\kappa_z,\omega) = {} & -i\frac{k_x^2+k_y^2}{2k_2(k_x,\omega)}A_2(k_x,k_y,\kappa_z,\omega) \\ & + \frac{i\omega^2}{2\epsilon_0 c^2 k_2(k_x,\omega)}P^{(2)}(k_x,k_y,k_2(k_x,\omega)+\kappa_z,\omega). \end{aligned} \tag{36}$$

Going back to real space for the z coordinate, we obtain

$$\begin{aligned} \frac{\partial A_2(k_x,k_y,z,\omega)}{\partial z} = {} & -i\frac{k_x^2+k_y^2}{2k_2(k_x,\omega)}A_2(k_x,k_y,z,\omega) \\ & + \frac{i\omega^2}{2\epsilon_0 c^2 k_2(k_x,\omega)}P^{(2)}(k_x,k_y,z,\omega)e^{-ik_2(k_x,\omega)z}. \end{aligned} \tag{37}$$

The resolution of this first-order differential equation is straightforward and yields the SHG envelope

$$\begin{aligned} A_2(k_x,k_y,z,\omega) = {} & \frac{i\omega^2}{2\epsilon_0 c^2 k_2(k_x,\omega)}\exp\left(-i\frac{k_x^2+k_y^2}{2k_2(k_x,\omega)}z\right) \\ & \int_0^z P^{(2)}(k_x,k_y,z',\omega)\exp\left(-ik_2(k_x,\omega)z' + i\frac{k_x^2+k_y^2}{2k_2(k_x,\omega)}z'\right)dz'. \end{aligned} \tag{38}$$

In order to calculate the integral along the z axis, we write the explicit expression of the second-order polarization by Fourier transforming the real-space expression $P^{(2)}(x,y,z,t) = \frac{1}{2}\epsilon_0\chi^{(2)}E_1(x,y,z,t)^2$, which yields the convolution product

$$\begin{aligned} P^{(2)}(k_x,k_y,z,\omega) = {} & \frac{\epsilon_0\chi^{(2)}}{2}\iiint E_1(k_{x1},k_{y1},z,\omega_1) \\ & E_1(k_x-k_{x1},k_y-k_{y1},z,\omega-\omega_1)\frac{dk_{x1}}{2\pi}\frac{dk_{y1}}{2\pi}\frac{d\omega_1}{2\pi}. \end{aligned} \tag{39}$$

Let us introduce the multidimensional wavevector mismatch function, defined as

$$\begin{aligned}\Delta k(k_x, k_{x1}, k_y, k_{y1}, \omega, \omega_1) = {} & k_1(\omega_1) + k_1(\omega - \omega_1) - k_2(k_x, \omega) \\ & - \frac{k_{x1}^2 + k_{y1}^2}{2k_1(\omega_1)} - \frac{(k_x - k_{x1})^2 + (k_y - k_{y1})^2}{2k_1(\omega_1)} + \frac{k_x^2 + k_y^2}{2k_2(k_x, \omega)}.\end{aligned} \tag{40}$$

At center frequency and with wavevectors aligned along the z axis, we have $\Delta k(0, 0, 0, 0, 2\omega_0, \omega_0) = 2k_1(\omega_0) - k_2(2\omega_0) = 0$, since we assume that phase matching is fulfilled. However, the mismatch function Δk will depart from zero for other frequency or wavevector values due to the finite spectral and angular acceptance of the phase-matching condition. Eq. (38) now becomes

$$\begin{aligned}A_2(k_x, k_y, z, \omega) = {} & \frac{i\omega^2 \chi^{(2)}}{4c^2 k_2(k_x, \omega)} \exp\left(-i\frac{k_x^2 + k_y^2}{2k_2(k_x, \omega)} z\right) \\ & \iiint E_1(k_{x1}, k_{y1}, \omega_1) E_1(k_x - k_{x1}, k_y - k_{y1}, \omega - \omega_1) \\ & \left(\int_0^z e^{i\Delta k(k_x, k_{x1}, k_y, k_{y1}, \omega, \omega_1) z'} dz'\right) \frac{dk_{x1}}{2\pi} \frac{dk_{y1}}{2\pi} \frac{d\omega_1}{2\pi}.\end{aligned} \tag{41}$$

The integration over z is straightforward and leads to the introduction of the multidimensional spatio-temporal global response function

$$\begin{aligned}\Xi(k_x, k_{x1}, k_y, k_{y1}, \omega, \omega_1) = {} & \frac{i\omega^2 \chi^{(2)}}{4c^2 k_2(k_x, \omega)} \exp\left(-i\frac{k_x^2 + k_y^2}{2k_2(k_x, \omega)} z\right) \\ & \frac{\exp\left(i\Delta k(k_x, k_{x1}, k_y, k_{y1}, \omega, \omega_1) z\right) - 1}{i\Delta k(k_x, k_{x1}, k_y, k_{y1}, \omega, \omega_1)},\end{aligned} \tag{42}$$

which is the spatio-temporal generalization of the global response function, previously introduced in frequency domain only. The second-harmonic field envelope now simply reads

$$\begin{aligned}A_2(k_x, k_y, z, \omega) = {} & \iiint \Xi(k_x, k_{x1}, k_y, k_{y1}, \omega, \omega_1) \\ & E_1(k_{x1}, k_{y1}, \omega_1) E_1(k_x - k_{x1}, k_y - k_{y1}, \omega - \omega_1) \frac{dk_{x1}}{2\pi} \frac{dk_{y1}}{2\pi} \frac{d\omega_1}{2\pi}.\end{aligned} \tag{43}$$

This expression allows to easily compute the SHG field for any spatio-temporal shape of the incident field. It can be easily simplified depending on actual experimental conditions. For example, if we except the case of tightly-focused beams [5] and assume that the crystal thickness is smaller than the confocal parameter, we can neglect diffraction terms in $k_x^2 + k_y^2$. The mismatch function then depends only on k_x (at first order), and on the frequency variables, with

$$\Delta k(k_x, \omega, \omega_1) = k_1(\omega_1) + k_1(\omega - \omega_1) - k_2(k_x, \omega). \tag{44}$$

This expression can be used to compute SHG taking into account walk-off, group-velocity mismatch and group-velocity dispersion (GVD). Additionally, neglecting GVD, we can use a first-order expansion of the wavevectors (Eq. (11) and (12)) and retrieve Eq. (13). Also, note that Eq. (42) can be simplified by neglecting the slow variation of $k_2(k_x, \omega)$ with respect to k_x and ω in the prefactor (but of course not in the phase term in Δk where the consequences of this variation are more dramatic). By setting $k_2 = n_2\omega/c$ in this prefactor, and neglecting diffraction, we thus easily recover Eq. (8) from Eq. (42).

Funding. Agence Nationale de la Recherche (ANR-21-CE30-0038-SHOTIME).

Disclosures. The authors declare no conflicts of interest.

Data Availability Statement. Data underlying the results presented in this article are not publicly available at this time but may be obtained from the authors upon reasonable request.

References

1. P. Franken, A. E. Hill, C. e. Peters, and G. Weinreich, “Generation of optical harmonics,” Phys. Rev. Lett. **7**, 118 (1961).
2. K. Tsubakimoto, H. Yoshida, and N. Miyanaga, “600 w green and 300 w UV light generated from an eight-beam, sub-nanosecond fiber laser system,” Opt. Lett. **42**, 3255–3258 (2017).
3. O. Novák, H. Turčičová, M. Smrž, T. Miura, A. Endo, and T. Mocek, “Picosecond green and deep ultraviolet pulses generated by a high-power 100 khz thin-disk laser,” Opt. Lett. **41**, 5210–5213 (2016).
4. J. Rothhardt, C. Rothhardt, M. Müller, A. Klenke, M. Kienel, S. Demmler, T. Elsmann, M. Rothhardt, J. Limpert, and A. Tünnermann, “100 w average power femtosecond laser at 343 nm,” Opt. Lett. **41**, 1885–1888 (2016).
5. D. A. Kleinman, A. Ashkin, and G. Boyd, “Second-harmonic generation of light by focused laser beams,” Phys. Rev. **145**, 338 (1966).
6. A. Smith, D. Armstrong, and W. Alford, “Increased acceptance bandwidths in optical frequency conversion by use of multiple walk-off-compensating nonlinear crystals,” JOSA B **15**, 122–141 (1998).
7. A. Weiner, A. Kan’an, and D. Leaird, “High-efficiency blue generation by frequency doubling of femtosecond pulses in a thick nonlinear crystal,” Opt. Lett. **23**, 1441–1443 (1998).
8. S. M. Saltiel, K. Koynov, B. Agate, and W. Sibbett, “Second-harmonic generation with focused beams under conditions of large group-velocity mismatch,” JOSA B **21**, 591–598 (2004).
9. H. Wang and A. M. Weiner, “Efficiency of short-pulse type-i second-harmonic generation with simultaneous spatial walk-off, temporal walk-off, and pump depletion,” IEEE Journ. Quant. Elec. **39**, 1600–1618 (2003).
10. Y. Takagi, Y. Yamada, K. Ishikawa, S. Shimizu, and S. Sakabe, “Ultrafast single-shot optical oscilloscope based on time-to-space conversion due to temporal and spatial walk-off effects in nonlinear mixing crystal,” Jap. Journ. Appl. Phys. **44**, 6546 (2005).
11. N. A. Chaitanya, A. Aadhi, R. P. Singh, and G. K. Samanta, “Type-i frequency-doubling characteristics of high-power, ultrafast fiber laser in thick bibo crystal,” Opt. Lett. **39**, 5419–5422 (2014).
12. N. A. Chaitanya, A. Aadhi, S. C. Kumar, M. Jabir, G. Samanta, and M. Ebrahim-Zadeh, “Frequency-doubling of femtosecond pulses in “thick” nonlinear crystals with different temporal and spatial walk-off parameters,” IEEE Phot. Journ. **8**, 1–13 (2016).
13. J. Hebling, “Derivation of the pulse front tilt caused by angular dispersion,” Opt. Quant. Elec. **28**, 1759–1763 (1996).
14. S. Akturk, X. Gu, P. Gabolde, and R. Trebino, “The general theory of first-order spatio-temporal distortions of gaussian pulses and beams,” Opt. Exp. **13**, 8642–8661 (2005).
15. R. Danielius, A. Piskarskas, P. Di Trapani, A. Andreoni, C. Solcia, and P. Foggi, “Matching of group velocities by spatial walk-off in collinear three-wave interaction with tilted pulses,” Opt. Lett. **21**, 973–975 (1996).
16. A. M. Schober, M. Charbonneau-Lefort, and M. M. Fejer, “Broadband quasi-phase-matched second-harmonic generation of ultrashort optical pulses with spectral angular dispersion,” JOSA B **22**, 1699–1713 (2005).
17. J. J. Huang, L. Y. Zhang, W. C. Zhang, S. R. Yan, S. Z. Pu, and W. X. Ren, “Theory of second harmonic generation of ultrashort pulses for collinear achromatic phase matching,” JOSA B **30**, 431–438 (2013).
18. B. Willenberg, F. Brunner, C. R. Phillips, and U. Keller, “High-power picosecond deep-uv source via group velocity matched frequency conversion,” Optica **7**, 485–491 (2020).
19. J. P. Torres, M. Hendrych, and A. Valencia, “Angular dispersion: an enabling tool in nonlinear and quantum optics,” Adv. Opt. Photon. **2**, 319–369 (2010).
20. P. Nuernberger, K. F. Lee, and M. Joffre, “Femtosecond spectroscopy from the perspective of a global multidimensional response function,” Acc. Chem. Res. **42**, 1433–1441 (2009).
21. M. Joffre, J. O. White, D. Hulin, A. Migus, E. Toussaere, R. Hierle, S. Gauvin, and J. Zyss, “Femtosecond ultrabroad-band frequency mixing in mna and kdp thin crystals,” Nonlinear Opt. **11**, 5–12 (1995).
22. L. Lepetit and M. Joffre, “Two-dimensional nonlinear optics using fourier-transform spectral interferometry,” Opt. Lett. **21**, 564–566 (1996).
23. N. Belabas and M. Joffre, “Visible-infrared two-dimensional fourier-transform spectroscopy,” Opt. Lett. **27**, 2043–2045 (2002).
24. T. Brabec and F. Krausz, “Nonlinear optical pulse propagation in the single-cycle regime,” Phys. Rev. Lett. **78**, 3282 (1997).
25. M. Hanna, X. Délen, L. Lavenu, F. Guichard, Y. Zaouter, F. Druon, and P. Georges, “Nonlinear temporal compression in multipass cells: theory,” J. Opt. Soc. Am. B **34**, 1340–1347 (2017).
26. T. Lang, A. Harth, J. Matyschok, T. Binhammer, M. Schultze, and U. Morgner, “Impact of temporal, spatial and cascaded effects on the pulse formation in ultra-broadband parametric amplifiers,” Opt. Exp. **21**, 949–959 (2013).